Nanoscale



PAPER View Article Online
View Journal | View Issue



Cite this: Nanoscale, 2020, 12, 12329

Ru and RuO_x decorated carbon nitride for efficient ammonia photosynthesis†

Hui Wang, D Xiyi Li, Qiushi Ruan D and Junwang Tang*

Photocatalytic ammonia synthesis is a promising strategy for sustainable development compared to the energy-intensive industrial Haber–Bosch approach. Herein, a ternary heterostructure that consists of ruthenium species and carbon nitride (C_3N_4) was rationally explored for ammonia photosynthesis. Compared to the small ammonia yield from the $g-C_3N_4$ and $Ru/g-C_3N_4$ system, the $Ru/RuO_2/g-C_3N_4$ system represents 6 times higher activity with excellent stability under full-spectrum irradiation. Such an enhancement is not only due to efficient transfer of electrons and holes to Ru and RuO_2 , respectively, facilitating both the reduction and oxidation reaction, but also taking advantage of Ru for $N \equiv N$ activation.

Received 30th March 2020, Accepted 1st May 2020 DOI: 10.1039/d0nr02527e

rsc.li/nanoscale

Introduction

Ammonia is one of the most fundamental and essential feedstocks in the chemical industry due to its application in fertilizer production, medicaments and biological molecules. ^{1,2} The main industrial process of ammonia production is the Haber-Bosch process, which requires extremely high temperatures and pressures, leading to an energy-intensive and highly carbon-emitting process. ³ Ammonia photosynthesis is believed to be a low cost and environmentally friendly approach which could be regarded as a promising next-generation ammonia synthesis technique. ^{4,5} However, the efficiency obtained to date has been very moderate, mainly due to the high recombination of photo-induced charges and the lack of efficient activation sites for cleavage of the N≡N triple bond.

Graphitic carbon nitride (g-C₃N₄), a thermally and chemically stable nitride semiconductor photocatalyst, is one of the most promising polymer photocatalysts for ammonia photosynthesis.^{6,7} It not only has good visible light absorption ability but also has enough driving force for the reduction reaction of N₂. Many g-C₃N₄ based photocatalysts, including g-C₃N₄/Cs_xWO₃, g-C₃N₄/ZrO₂, g-C₃N₄/ZnMoCdS ¹⁰ and so on, have been applied in ammonia photosynthesis. However, they mainly suffered from low efficiency of charge separation, thus resulting in a low yield in photocatalytic N₂ reduction. Engineering heterojunctions has been proved to be one of the most effective ways for the spatial separation of photo-induced

Solar Energy & Advanced Materials Research Group, Department of Chemical Engineering, UCL, Torrington Place, London, WC1E 7JE, UK.
E-mail: iumwane.tane@ucl.ac.uk

†Electronic supplementary information (ESI) available. See DOI: 10.1039/d0nr02527e

carriers. 11,12 Besides, the precise design of suitable active sites and matching of functionalities during heterojunction construction certainly aid in the specific photocatalytic reaction. 13 Experimental and theoretical studies indicated that N_2 could be easily adsorbed and activated on the Ru catalyst surface to form N_2H_x species to facilitate the cleavage of the $N\equiv N$ triple bonds in thermal catalysis. 14,15 Recently, Ru has been used as an efficient cocatalyst for photo-assisted ammonia synthesis in aqueous solutions such as Ru/GaN and Ru/TiO₂ due to the electron trapping sites of Ru. 16,17 It is more efficient if a dual cocatalyst could be loaded for efficient trapping of both electrons and holes and also facilitate both reduction and oxidation reactions.

Ruthenium oxide (RuO2) has been widely reported to be efficient as a hole acceptor, specifically it could extract photogenerated holes from excited photocatalysts efficiently and therefore suppresses charge recombination. Hence, it is of particular interest to rationally design the Ru/RuO₂/g-C₃N₄ ternary heterojunction by coating RuO2 and Ru clusters on g-C3N4 nanosheets as dual co-catalysts for efficient ammonia photosynthesis. The 2D g-C₃N₄ nanosheets, with short bulk-tosurface diffusion length, accelerate the transfer of photoinduced carriers. Moreover, it also provides large surface area and abundant unsaturated sites (e.g. -NH₂) for coordination of active components. Based on this excellent platform, the suitable choice of Ru as an electron acceptor not only takes advantage of its unique interaction and activation with N≡N, but also makes good use of the formed oxide species (RuO2) as a well-known hole acceptor. This ternary heterostructure Ru/ RuO₂/g-C₃N₄ exhibits a much higher NH₃ generation rate (13.3 μ mol g⁻¹ h⁻¹) than Ru/g-C₃N₄ (2.5 μ mol g⁻¹ h⁻¹) and g-C₃N₄ (almost zero). The optimised catalyst can also remain stable for at least four cycles.

2. Experimental section

g-C₃N₄ was synthesized using urea as the precursor. In detail, 10 g urea powder was calcined in a muffle furnace (Carbolite, CWF 1300) at 550 °C for 4 h with a rate of 5 °C min⁻¹. The obtained vellow product was washed with water, 0.1 M HCl, 0.1 M NaOH and water three times, respectively, then dried in an oven at 70 °C overnight. RuO2 and/or Ru loaded carbon nitride was synthesized via wet impregnation. Typically, 200 mg bulk C₃N₄ and 45 wt% RuCl₃·H₂O were suspended in 40 ml water followed by ultra-sonication (Fisherbrand) for 30 min. After that, the suspension was dried at 100 °C and calcined at 300 °C for 2 h in air and under a 10% H₂/Ar atmosphere, and were labelled as Ru/RuO₂/g-C₃N₄ and Ru/g-C₃N₄, respectively. Ru loaded on g-C₃N₄ by photodeposition was labelled as Ru/ g-C₃N₄-p. The obtained materials were washed several times with water to remove RuCl3 residues. A series of Ru/RuO2/ $g-C_3N_4$ samples were labelled as Ru/RuO₂/ $g-C_3N_4$ -5% x% (x = 0.5-7.5), where x is the Ru loading weight percentage (nominal ratio).

The powder X-ray diffraction (XRD) was carried out using a Bruker D4 diffractometer equipped with a Cu-K α source (K α 1 = 1.540562 Å and $K\alpha 2 = 1.544398$ Å). Transmission electron microscopy (TEM) (JEOL2010) was used to analyse the morphology and composition of the sample. The surface elemental composition analyses was characterized by X-ray Photoelectron Spectroscopy (XPS) (Thermoscientific XPS K-alpha). UV-vis-NIR diffuse reflectance spectra (DRS) were recorded using an Agilent Carry 3500 UV-Vis-NIR spectrophotometer equipped with a diffuse reflectance unit. Steady-state photoluminescence (PL) and Raman spectra were examined using a Renishaw inVia Raman microscope. Photocurrent testing was carried out using a closable three-electrode electrolytic cell, using an electrochemical workstation (IVIUM) control voltage with 0.1 mol L⁻¹ Na₂SO₄ solution as the electrolyte, where the FTO electrode coated with the catalyst was used as the working electrode, the platinum plate was used as the counter electrode, and the Ag/AgCl electrode was used as the reference electrode.

In a typical photocatalytic N_2 reduction reaction, a certain amount of photocatalyst was well dispersed in 30 ml of aqueous solution containing a sacrificial electron donor and then transferred to a 100 ml reactor. An in-house-built 100 mL two-necked flat-bottomed quartz container was used as the reactor, 50 mL of deionized water was used as the solvent and proton source for the reaction, and 0.03 g of the obtained photocatalyst was added into the solution. The reactor was sealed, purged with N_2 gas for 20 min and then irradiated. The N_2 and Ar control experiment was irradiated under LED irradiation (365 nm). Other control and cycling experiments were irradiated under full arc using a 300 W xenon lamp. The solution was taken out at regular intervals to detect ammonia concentration using ion chromatography.

Photocurrent testing was carried out using a three-electrode electrolytic cell, using an electrochemical workstation (IVIUM) control voltage. $0.1~M~Na_2SO_4$ solution was used as the electrolyte, the FTO electrode coated with the catalyst was used as the

working electrode, the platinum plate served as the counter electrode, and the Ag/AgCl electrode acted as the reference electrode. A 150 W xenon lamp was used as the full arc light source. The photocurrent test was carried out using a potentiostatic technique with a switching period of 5 s, which mainly measured the photocurrent density of the photocatalysts. The alternating current impedance spectrum was measured using a three-electrode system with the following parameters: at -0.4 V vs. Ag/AgCl, high frequency 10 kHz, low-frequency 1 Hz, amplitude 10 mV. The test was carried out under irradiation with 100 mL of 0.1 M Na₂SO₄ solution as the electrolyte.

3. Results and discussion

The crystal structure of the obtained samples along with pure carbon nitride was firstly examined by powder X-ray diffraction (Fig. 1a). The characteristic diffraction peak at 27.4° assigned to the interlayer stacking of g-C3N4 in all three samples remains unchanged, excluding the insertion of Ru species at the interlayer. 18 The Ru/g-C₃N₄-5% sample shows a series of peaks at 38.0°, 41.9°, 43.6°, 57.8°, 68.7° and 77.7° which are ascribed to the $(1\ 0\ -1\ 0)$, $(0\ 0\ 0\ 2)$, $(1\ 0\ -1\ 1)$, $(1\ 0\ -1\ 2)$, $(2\ -1\ 0)$ -1 0) and (1 0 -1 3) lattice planes of the hexagonal Ru crystal structure, which corresponds to the commercial Ru. In contrast, no peaks attributed to RuOx species can be observed over the Ru/RuO₂/g-C₃N₄-5% sample which may be due to the low amount or high dispersion of Ru species. FTIR and Raman spectroscopy were used to characterize the stable chemical structure of the obtained samples. For FTIR spectra (Fig. 1b), the typical signal at 810 cm⁻¹ is assigned to the out-of-plane bending vibration characteristic of heptazine. The multiple peaks at 1200-1600 cm⁻¹ represent the stretching vibration of tri-s-triazine heterocyclic stretches. 19 Moreover, the absorption

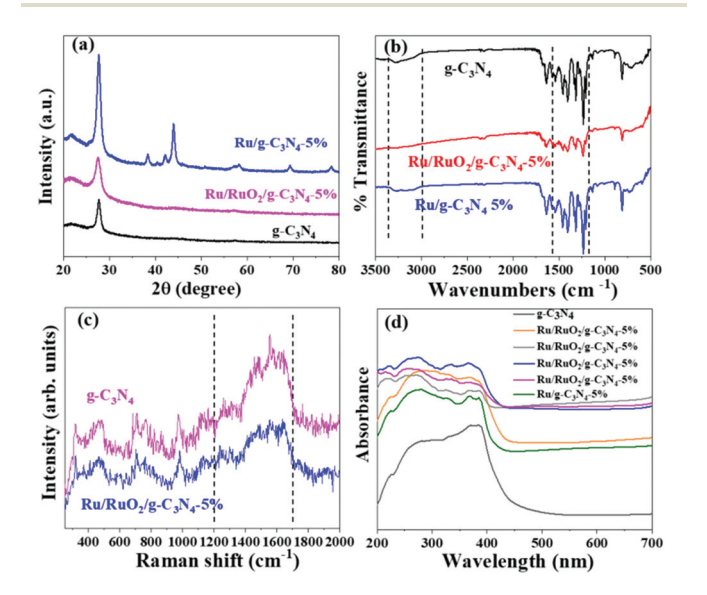


Fig. 1 XRD patterns (a), FTIR spectra (b), Raman spectra (c), and UV-Vis spectra (d) of $g-C_3N_4$, $Ru/RuO_2/g-C_3N_4-5\%$ and $Ru/g-C_3N_4-5\%$.

Nanoscale Paper

band in the range of 3000-3300 cm⁻¹ is ascribed to the -NH₂ stretching. 18 Raman spectroscopy was carried out to examine the fine structure of g-C₃N₄ and Ru/RuO₂/g-C₃N₄-5% in detail (Fig. 1c). In the range of 1200–1700 cm⁻¹, a series of peaks are attributed to C-N stretching vibrations, specifically "G" and "D" band profiles of structurally disordered graphitic carbon and other carbon/nitrogen layered compounds. 20,21 The peak at 980 cm⁻¹ could be assigned to the symmetric N-breathing mode of heptazine, whilst the peak at 690 cm⁻¹ corresponds to the in-plane bending vibrations of the tri/heptazine C-N-C linkages.²² All the above characterizations confirm the preservation of carbon nitride's structure after loading Ru species, while the specific peaks assigned to Ru species are not observed, again due to the highly dispersed and low amount of Ru loaded. 23,24

TEM was applied to analyse the microstructures of photocatalysts after loading Ru and RuO2 (Fig. 2). The thin g-C3N4 nanosheets are firmly assembled with small nanoparticles, constructing stable 0D/2D heterojunctions. The size of Ru species is around 2 nm, as shown in Fig. S1.† Fig. 2b shows the high-resolution image along with the fast Fourier transform (FFT) image. The transformed lattice fringe with a spacing of 0.207 nm matches well with the (101) plane of the metallic Ru, while the spacing of 0.18 nm corresponds to the (211) lattice plane of RuO₂. ^{25,26} Ru and RuO₂ formation was believed to be due to calcination of the Ru precursor on carbon nitride at 300 °C in air. Similarly, the formation of Ru and RuO2 by thermal decomposition in air was reported, where a mixture of RuO2 as the dominant phase and Ru was found in the sample to be calcined between 200 °C and 400 °C.27 The reason is likely due to the organic substrate working as a reductant.²⁸ The EDS mapping (Fig. 2c) shows

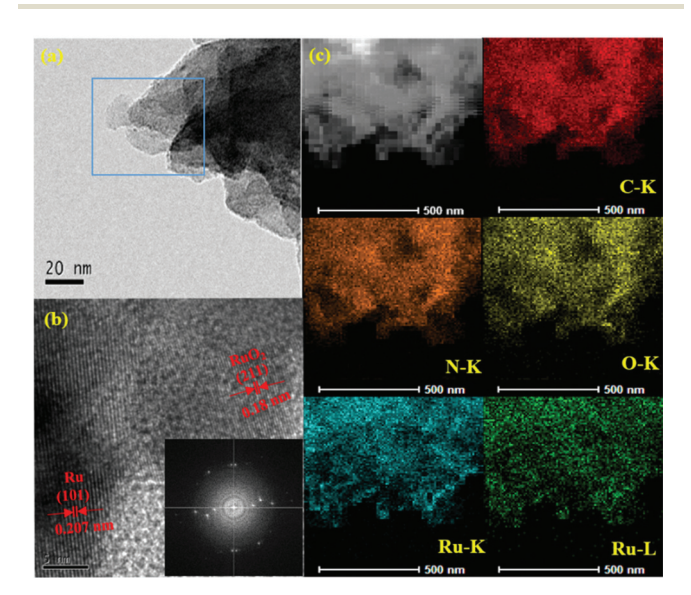


Fig. 2 TEM (a), the diffraction pattern of the selected area (b) and the corresponding elemental mapping images (c) of Ru/RuO₂/q-C₃N₄-5% nanosheets. The inset in (b) is the corresponding fast Fourier transform image.

the homogeneous distribution of the corresponding elements (C, N, O and Ru), indicating the high dispersion of RuO_x on the g-C₃N₄. The high dispersion of Ru species can be attributed to two reasons: (i) long duration of sonication can help disperse the Ru precursor during uniform precipitation on the carbon nitride; (ii) carbon nitride possesses rich NH₂- groups, which are widely reported to coordinate and anchor transition metals, avoiding the aggregation. Furthermore, Ru and O are ubiquitously dispersed in the selected region of Ru/RuO2/ g-C₃N₄-5%, indicating successful formation of RuO_x.

To further investigate the chemical states of Ru species in the as-prepared sample, X-ray photoelectron spectroscopy (XPS) measurement was carried out (Fig. 3). The C 1s spectra overlap with Ru 3d spectra (Fig. 3a), illustrating three main peaks at 288.0 eV, 286.2 eV and 284.6 eV corresponding to the sp²-bonded carbon (N-C=N), C-O and adventitious C-C bond, respectively.²⁹ The signals at 280.2 eV and 281.7 eV are ascribed to Ru⁰ and RuO₂, respectively.³⁰ The peaks in N 1s spectra (Fig. 3b) at 398.5 eV and 400.0 eV are assigned to heptazine C-N-C and N-(C)3, while the signal centred at 401.2 eV corresponds to the C-N-H bond. In order to unravel the coexistence of Ru and RuO2, we further analysed the Ru species by XPS (Fig. 3c). The peaks at 461.9 eV and 484.1 eV are assigned to metallic Ru, while those at 463.7 eV and 485.9 eV are correlated to RuO₂. 31,32 The average ratio of Ru⁰/RuO₂ in Ru/RuO₂/ g-C₃N₄ is calculated to be 0.18 by the curve fit of Ru 3p spectra. The peaks at 531.2 eV and 532.3 eV in O 1s spectra are related to Ru-O-Ru and -C-O, respectively. The binding energy at 534 eV is assigned to the adsorbed H₂O (Fig. 3d).³³ In addition, the XPS Ru 3p spectra of Ru/RuO₂/g-C₃N₄-5% and Ru/g-C₃N₄-5% are shown in Fig. S2.† Compared with the Ru 3p spectra of Ru/RuO₂/g-C₃N₄-5%, Ru/g-C₃N₄-5% shows peaks at 461.9 eV and 484.2 eV, corresponding to Ru $3p_{3/2}$ and Ru $3p_{1/2}$ of metallic Ru. The absence of RuO₂ in Ru/g-C₃N₄-5% is due to

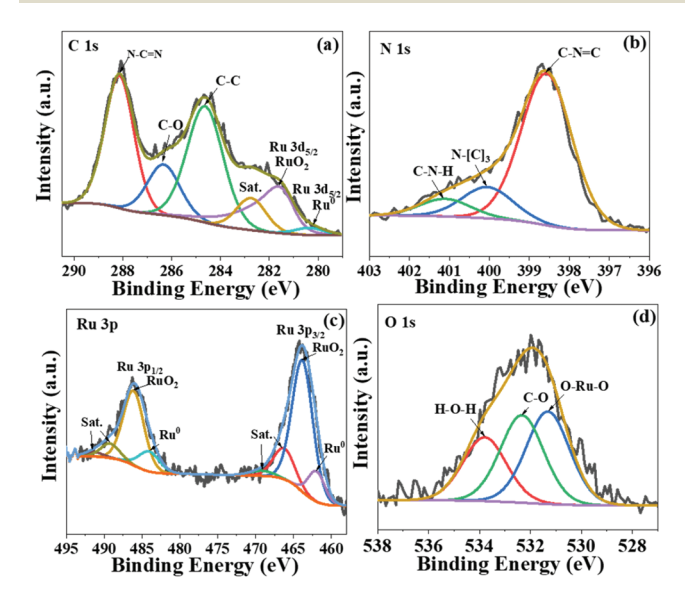


Fig. 3 The C 1s (a), N 1s (b), Ru 3p (c), and O 1s (d) XPS spectra of Ru/ $RuO_2/g-C_3N_4-5\%$.

Paper Nanoscale

the reduction condition of H₂. Combining the TEM and XPS analysis of the Ru/RuO₂/g-C₃N₄-5% sample, Ru species exist as Ru and RuO2 clusters on carbon nitride nanosheets.

The photocatalytic activity for ammonia synthesis is shown in Fig. 4. Control experiments were conducted and are shown in Fig. 4a. No ammonia is detected from the pure g-C₃N₄ and in the absence of illumination, indicating that the Ru species and light irradiation are both indispensable to the photocatalytic ammonia photosynthesis. A small concentration of 15 μmol g⁻¹ NH₄⁺ was initially observed in the Ru/RuO₂/ g-C₃N₄-5% sample under an Ar atmosphere while no further increase of NH₄⁺ can be observed in the following 5 hours. The production of NH₄⁺ in the first hour is likely due to the remaining NH_x species adsorbed on g-C₃N₄ during sample preparation rather than photosynthesis of N2. In the absence of the Ru cocatalyst, this adsorbed NHx cannot be easily desorbed, while with the loading of the Ru cocatalyst, this small amount of adsorbed NH_x is readily removed within one hour. This is an interesting note for ammonia synthesis if there were NH_x groups produced during photocatalyst synthesis. When changing to a N2 atmosphere, the ammonia yield on the Ru/ RuO₂/g-C₃N₄-5% sample linearly increases, on average 13.3 μ mol g⁻¹ h⁻¹, indicating that N₂ gas is the main source of ammonia photosynthesis. Then, the Ru cocatalyst amount was investigated between 0.5 wt% and 7.5 wt% to optimise its loading. All samples present enhanced activity compared with pure C₃N₄. The optimum amount of the loaded co-catalyst has been determined to be 5%, showing the highest N2 fixation activity with an NH₄⁺ concentration of 13.3 µmol g⁻¹ h⁻¹ under full arc irradiation. The ammonia generation rate is

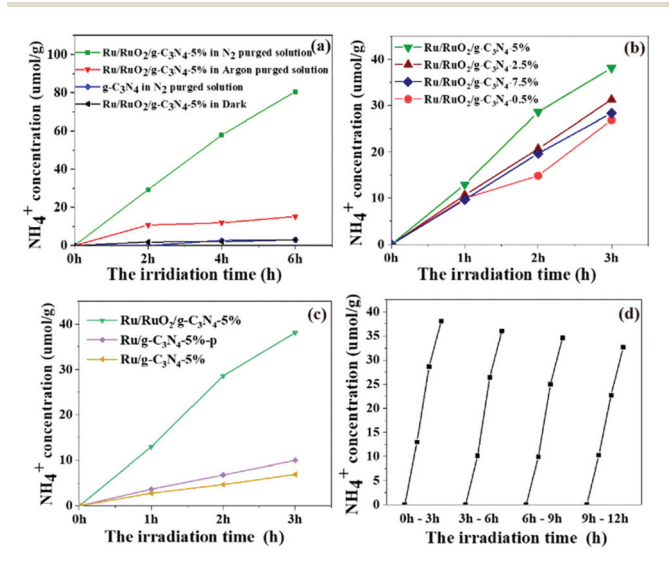


Fig. 4 The photocatalytic N₂ reduction and control experiments by Ru/ RuO₂/g-C₃N₄-5% under 365 nm LED illumination (a), photocatalytic ammonia yield of Ru/RuO₂/g-CN₄ with co-catalyst loading (0.5 wt%-7.5 wt%) in N₂ purged water under full arc irradiation (b), photocatalytic activity of $Ru/RuO_2/g-C_3N_4-5\%$, $Ru/g-C_3N_4-5\%-p$ and $Ru/g-C_3N_4-5\%$ (c), and photocatalytic cycling tests for Ru/RuO₂/g-C₃N₄-5% in N₂ purged water under full arc irradiation (d). All experiments were carried out under neutral conditions with a pH value of 7.

comparable to that of the reported Ru system photocatalysts which have been list in Table S1.† 34,35 A further increase in the amount of loaded co-catalysts results in decreased activity, because excess co-catalyst may block the light absorption of g-C₃N₄.³⁶ In order to elucidate the important role of RuO₂ in ternary heterostructures, other methods including photodeposition and H2 reduction have been used to load Ru species on g-C₃N₄ (denoted Ru/g-C₃N₄-5%-p and Ru/g-C₃N₄-5%) for comparison (Fig. 4c). All samples exhibited a linear increase in ammonia production with increasing time. Ru/g-C₃N₄-5% and Ru/g-C₃N₄-5%-p present an ammonia yield of less than 10 μmol g⁻¹ after 3 h full arc irradiation, only one-fourth of that achieved by Ru/RuO₂/g-C₃N₄-5%. On the former samples, only Ru metallic species were observed as mentioned above, which can act as an electron acceptor and activation sites for N₂ reduction. 12 The extraordinary high activity of Ru/RuO₂/ g-C₃N₄-5% can be ascribed to the synergistic effect between metallic Ru and RuO2 on g-C3N4 for both electron and hole extraction as well as for N2 activation as discussed below. In addition, a little change is observed from cycling experiments in Fig. 3d, which is believed to be due to the loss of a photocatalyst amount as we filtered the sample from the solution for cycling. Furthermore, the XRD and XPS of Ru/RuO₂/g-C₃N₄-5% before and after the reaction are presented in Fig. S3 and Fig. S4.† No obvious differences in the XRD peaks and Ru 3p XPS spectra of the used photocatalyst are observed compared with that of the fresh photocatalyst. The ratio of the Ru metal and RuO₂ before and after the reaction has been compared to further confirm the stability of Ru/RuO₂/g-C₃N₄-5%. The Ru/ RuO₂ ratio after the reaction is estimated to be 0.19, which is similar to that before the reaction (0.20). All these results prove that the two cocatalysts remain very stable.

UV-Vis DRS analysis was implemented to investigate the light absorption of all samples (Fig. 1d). g-C₃N₄ exhibits light absorption from the UV to visible range, and the sharp edge suggests that the visible light absorption is due to the band gap transition. After loading Ru species, there is no obvious difference in the absorption edge compared with the pristine g-C₃N₄, indicating that loading Ru and RuO₂ does not have a great influence on the band structure of g-C₃N₄. In the visible light region, the light absorption intensities of Ru/g-C₃N₄-5% and Ru/RuO₂/g-C₃N₄-5% samples are strengthened gradually as Ru species increase, which may be due to the light scattering of the Ru species. Photoluminescence (PL) spectra of the samples were recorded to study the behaviour of photogenerated charge carriers, shown in Fig. 5a. The g-C₃N₄ exhibits broad and robust doublet peaks at 440 nm and 500 nm. The emission centre at around 440 nm is ascribed to π - π * transitions, which are usually observed in conjugated ring systems including heterocyclic aromatic compounds. The peak at around 500 nm is explained as the n- π^* transition, 37 which involves lone pairs on the N atom on the edge of the triazine/ heptazine ring. After introducing Ru species, Ru/g-C₃N₄-5% exhibits a similar emission peak profile to that of pure g-C₃N₄ with decreased intensity. Ru/RuO₂/g-C₃N₄-5% also shows the same trend but the lowest intensity compared with Ru/g-C₃N₄

Nanoscale Paper

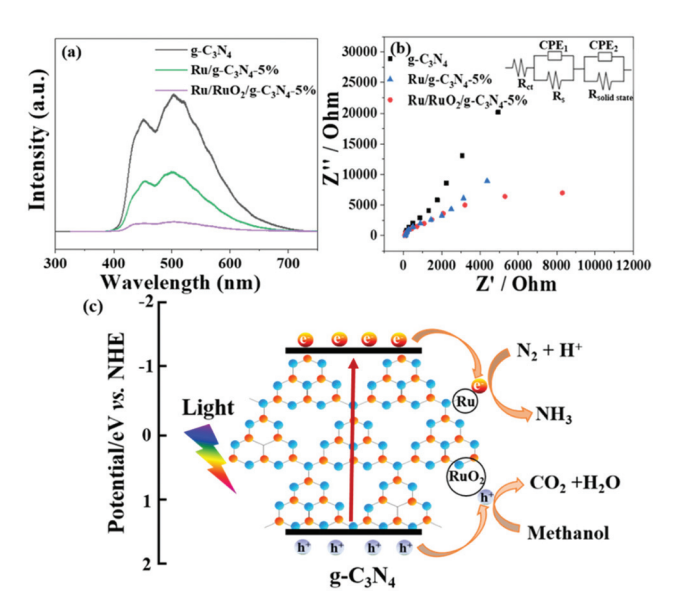


Fig. 5 The photoluminescence (a) and EIS (b) of $Ru/RuO_2/g-C_3N_4-5\%$ and $g-C_3N_4$ (inset is the interface charge transfer by fitting the impedance plots). A potential mechanism for the ammonia photosynthesis activity of $Ru/RuO_2/g-C_3N_4-5\%$ (c).

and g- C_3N_4 , indicating the least charge carrier recombination in the Ru/RuO₂/g- C_3N_4 sample.

To investigate charge transfer kinetics among different samples, in situ photoelectrochemical and electrochemical impedance spectroscopy measurements were performed on all three samples in N₂ purged solution. From Fig. S5,† Ru/RuO₂/ g-C₃N₄-5% exhibits higher reduction photocurrent density (e.g. $2 \mu A cm^{-2}$) compared to Ru/g-C₃N₄-5% (0.6 $\mu A cm^{-2}$). It is consistent with the enhanced NH3 evolution rate on Ru/RuO2/ g-C₃N₄-5% compared with that on Ru/g-C₃N₄-5%. Pure g-C₃N₄ has shown negligible photocurrent density, which also maintains consistency with its negligible NH3 synthesis performance. The interface charge transfer of all three samples was described by fitting the impedance scan plots to the equivalent circuit shown in the inset of Fig. 5b. The equivalent circuit model consists of two components: the electrode/electrolyte interface impedance (Rct and CPE1) and solid-state interface impedance ($R_{\text{solid-state}}$ and CPE_2). R_s is the system resistance, $R_{\rm ct}$ is the electrode/electrolyte interface charge transfer resistance and R_{solid-state} is the solid-state interface (e.g. g-C₃N₄/ RuO2 and g-C3N4/Ru) charge transfer resistance, respectively. The results summarized in Table 1 show that all three samples have a similar system resistance around 40 Ω cm². However, charge transfer resistance (Rct) dramatically differs among different samples. Obviously, co-catalyst (Ru/RuO2 or Ru) loading has essentially reduced the electrode/electrolyte interface charge transfer resistance, as R_{ct} has decreased from 2.46 \times 10⁶ Ω cm² of g-C₃N₄ to 9.8 \times 10³ Ω cm² of Ru/RuO₂/g-C₃N₄-5% and 3.38 \times 10⁴ Ω cm² of Ru/g-C₃N₄-5%. The reduced charge transfer resistance or enhanced charge transfer is attributed to the presence of metallic Ru and RuO2. In consequence, g-C₃N₄ has shown negligible NH₃ production and

Table 1 The interface charge transfer resistances and CPE of $g-C_3N_4$, $Ru/RuO_2/g-C_3N_4-5\%$ and $Ru/g-C_3N_4-5\%$

| | g-C ₃ N ₄ | Ru/g-C ₃ N ₄ - 5% | Ru/RuO ₂ /g-C ₃ N ₄ - 5% |
|--|--|---|--|
| $R_{\rm s} (\Omega \text{ cm}^2)$ $R_{\rm ct} (\Omega \text{ cm}^2)$ $CPE_1 (S^n \Omega^{-1} \text{ cm}^{-2})$ $R_{\rm solid-state} (\Omega \text{ cm}^2)$ $CPE_2 (S^n \Omega^{-1} \text{ cm}^{-2})$ | 42.5 2.46×10^{6} 1.02×10^{-4} 2.21×10^{2} 2.12×10^{-4} | 45.9 9.8×10^{3} 1.63×10^{-4} 1.82×10^{3} 1.63×10^{-4} | 36.8 3.38×10^{4} 4.02×10^{-4} 1.74×10^{3} 3.25×10^{-4} |

photocurrent in part due to a high charge transfer resistance, while $Ru/RuO_2/g$ - C_3N_4 -5% and Ru/g- C_3N_4 -5% exhibit significant NH_3 synthesis activities of 13.3 μ mol g^{-1} h^{-1} and 2.5 μ mol g^{-1} h^{-1} , respectively.

Apart from the solid-solution interface, charge transfer at the solid-state interface is also imperative in deciding the photocatalytic activity. To be precise, the solid-state interface charge transfer resistances ($R_{\rm solid-state}$) are $2.21 \times 10^2~\Omega~{\rm cm}^2$ on g-C₃N₄, $1.74 \times 10^3~\Omega~{\rm cm}^2$ on Ru/RuO₂/g-C₃N₄ 5% and $1.82 \times 10^4~\Omega~{\rm cm}^2$ on Ru/g-C₃N₄-5%. As $R_{\rm solid-state}$ represents the resistance between g-C₃N₄/g-C₃N₄, RuO₂/g-C₃N₄ or Ru/g-C₃N₄ particle boundaries, their smaller values compared to the solid-solution interface resistance confirmed over 5 times faster solid-solid charge transfer than the solid-solution charge transfer. One can see the increased $R_{\rm solid-state}$ value on Ru/RuO₂/g-C₃N₄-5%, indicating that the enhanced activity is in part due to the improved charge transfer between the catalyst and solution instead of between C₃N₄ particles.

Based on the above characterization and experimental results, a possible ammonia synthesis mechanism is proposed on the best sample of Ru/RuO₂/g-C₃N₄-5% (Fig. 5c). When irradiated, electrons can be excited from the valence band to the conduction band of g-C₃N₄, which are further trapped by metallic Ru as the electrons sink. Then, these electrons are transferred from the Ru to the π antibonding orbital of N₂, facilitating the cleavage of the N \equiv N triple bonds, thus activating N₂. The activated N₂ on the Ru catalyst surface further reacts with H⁺ in water to form NH₃, and finally forms NH₄⁺ in water. Meanwhile, the left holes are transported to RuO₂ and scavenged by methanol, leading to a decrease of the electronhole recombination.

Conclusions

In summary, the ternary heterostructure $Ru/RuO_2/g$ - C_3N_4 system was explored and it exhibited excellent photocatalytic N_2 reduction activity and stability under full arc irradiation. It was found that g- C_3N_4 has shown negligible activity, while Ru-g- C_3N_4 and Ru/RuO_2 -g- C_3N_4 yielded 2.5 μ mol g^{-1} h⁻¹ and 13.3 μ mol⁻¹ g h⁻¹ ammonia under full arc irradiation, respectively. The resulting structure was characterized by XRD, Raman, FTIR and TEM. The electron transfer mechanism was confirmed by spectroscopy including PL and PEC. The higher activity of $Ru/RuO_2/g$ - C_3N_4 over Ru-g- C_3N_4 illustrated the

Paper Nanoscale

imperative role of RuO2 in enhancing the N2 fixation efficiency of g-C₃N₄. More importantly, a large amount of electrons trapped on Ru enhanced the electron transfer to the antibonding orbital of N₂, leading to N₂ activation. Hence, the synthetic strategy to incorporate both Ru and RuO2 to form the ternary system, where Ru acts as N₂ adsorption and activation sites for the reduction reaction and RuO2 serves as fast hole extraction sites for the oxidation reaction, leads to the enhanced photocatalytic activity.

Conflicts of interest

There are no conflicts to declare.

Acknowledgements

H. W. acknowledges the support from the UCL Dean's prize and China CSC scholarship. We all gratefully acknowledge the financial support provided by the UK EPSRC (EP/N009533/1), Royal Society-Newton Advanced Fellowship (NA170422) and the Leverhulme Trust (RPG-2017-122).

Notes and references

- 1 S. Vaclav, Detonator of the population explosion, Nature, 1999, 400, 415.
- 2 R. Raja, G. Sankar and J. M. Thomas, Bifunctional Molecular Sieve Catalysts for the Benign Ammoximation of Cyclohexanone: One-Step, Solvent-Free Production of Oxime and \varepsilon-Caprolactam with a Mixture of Air and Ammonia, J. Am. Chem. Soc., 2001, 123, 8153-8154.
- 3 S. Licht, S. B. Cui, B. Wang, F. Li, J. Lau and S. Liu, Ammonia synthesis by N2 and steam electrolysis in molten hydroxide suspensions of nanoscale Fe₂O₃, Science, 2014, **345**, 637-640.
- 4 N. Zhang, A. Jalil, D. Wu, S. Chen, S. Chen, Y. i. Liu, C. Gao, W. Ye, Z. Qi, H. Ju, C. Wang, X. Wu, L. Song, J. Zhu and Y. Xiong, Refining Defect States in W₁₈O₄₉ by Mo Doping: A Strategy for Tuning N2 Activation towards Solar-Driven Nitrogen Fixation, J. Am. Chem. Soc., 2018, 140, 9434-9443.
- 5 H. Hirakawa, M. Hashimoto, Y. Shiraishi and T. Hirai, Photocatalytic Conversion of Nitrogen to Ammonia with Water on Surface Oxygen Vacancies of Titanium Dioxide, J. Am. Chem. Soc., 2017, 139, 10929-10936.
- 6 H. Liu, P. Wu, H. Lia, Z. Chen, L. Wang, X. Zeng, Y. Zhu, Y. Jiang, X. Liao, B. S. Haynes, J. Yee, C. Stampfl and J. Huang, Unravelling the effects of layered supports on Ru nanoparticles for enhancing N₂ reduction in photocatalytic ammonia synthesis, Appl. Catal., B, 2019, 259, 118026.
- 7 Y. Shiraishi, S. Shiota, Y. Kofuji, M. Hashimoto, K. Chishiro, H. Hirakawa, S. Tanaka, S. Ichikawa and T. Hirai, Nitrogen fixation with water on carbon-nitridebased metal-free photocatalysts with 0.1%

- ammonia Energy Conversion Efficiency, ACS Appl. Energy Mater., 2018, 1, 4169-4177.
- 8 A. Shi, H. Li, S. Yin, Z. Hou, J. Rong, J. Zhang and Y. Wang, Photocatalytic NH₃ versus H₂ evolution over g-C₃N₄/ Cs_xWO₃: O₂ and methanol tipping the scale, Appl. Catal., B, 2018, 235, 197-206.
- 9 H. Mou, J. Wang, D. Yu, D. Zhang, W. Chen, Y. Wang, D. Wang and T. Mu, Fabricating Amorphous g-C₃N₄/ZrO₂ Photocatalysts by One-Step Pyrolysis for Solar-Driven Ambient Ammonia Synthesis, ACS Appl. Mater. Interfaces, 2019, 11, 44360-44365.
- 10 Q. Zhang, S. Hu, Z. Fan, D. Liu, Y. Zhao, H. Ma and F. Li, Preparation of g-C₃N₄/ZnMoCdS hybrid heterojunction catalyst with outstanding nitrogen photofixation performance under visible light via hydrothermal post-treatment, Dalton Trans., 2016, 45, 3497-3505.
- Marschall, Semiconductor composites: Strategies for enhancing charge carrier separation to improve photocatalytic activity, Adv. Funct. Mater., 2014, 24, 2421-2440.
- 12 X. Wang, C. Liow, A. Bisht, X. Liu, T. C. Sum, X. Chen and S. Li, Engineering Interfacial Photo-Induced Charge Transfer Based on Nanobamboo Array Architecture for Efficient Solar-to-Chemical Energy Conversion, Adv. Mater., 2015, 27, 2207-2214.
- 13 H. Wang, L. Zhang, Z. Chen, J. Hu, S. Li, Z. Wang, J. Liu and X. Wang, Semiconductor heterojunction photocatalysts: Design, construction, and photocatalytic performances, Chem. Soc. Rev., 2014, 43, 5234-5244.
- 14 H. Duan, J. Liu, M. Xu, Y. Zhao, X. Ma, J. Dong, X. Zheng, J. Zheng, C. S. Allen, M. Danaie, Y. Peng, T. Issariyakul, D. Chen, A. I. Kirkland, J. Buffet, J. Li, S. C. E. Tsang and D. O'Hare, Molecular nitrogen promotes catalytic hydrodeoxygenation, Nat. Catal., 2019, 2, 1078-1087.
- 15 K. Honkala, A. Hellman, I. N. Remediakis, A. Logadottir, A. Carlsson, S. Dahl, C. H. Christensen and J. K. Nørskov, Ammonia Synthesis from First-Principles Calculations, Science, 2005, 307, 555-558.
- 16 L. Li, et al., Nitrogen Photofixation over III-Nitride Nanowires Assisted by Ruthenium Clusters of Low Atomicity, Angew. Chem., Int. Ed., 2017, 56, 8701–8705.
- 17 K. T. Ranjit and B. Viswanathan, Photocatalytic reduction of dinitrogen to ammonia, Indian J. Chem., 1996, 35, 443-
- 18 X. Wang, X. Chen, A. Thomas, X. Fu and M. Antonietti, Metal-containing carbon nitride compounds: a new functional organic-metal hybrid material, Adv. Mater., 2009, 21, 1609-1612.
- 19 J. Oh, J. Lee, J. C. Koo, H. R. Choi, Y. Lee, T. Kim, N. D. Luong and J. Nam, Graphene oxide porous paper from amine-functionalized poly(glycidyl methacrylate)/graphene oxide core-shell microspheres, J. Mater. Chem., 2010, 20, 9200-9204.
- 20 A. C. Ferrari and J. Robertson, Interpretation of Raman spectra of disordered and amorphous carbon, Phys. Rev. B: Condens. Matter Mater. Phys., 2000, 61, 14095-14107.

Nanoscale

21 A. B. Jorge, D. J. Martin, M. T. S. Dhanoa, A. S. Rahman, N. Makwana, J. Tang, A. Sella, F. Corà, S. Firth, J. A. Darr and P. F. McMillan, H₂ and O₂ Evolution from Water Half-Splitting Reactions by Graphitic Carbon Nitride Materials, J. Phys. Chem. C, 2013, 117, 7178–7185.

- 22 P. J. Larkin, M. P. Makowski and N. B. Colthup, The form of the normal modes of s-triazine: Infrared and Raman spectral analysis and ab initio force field calculations, *Spectrochim. Acta, Part A*, 1999, 55, 1011–1020.
- 23 M. Xiao, L. Gao, Y. Wang, X. Wang, J. Zhu, Z. Jin, C. Liu, H. Chen, G. Li, J. Ge, Q. He, Z. Wu, Z. Chen and W. Xing, Engineering energy level of metal center: Ru single-atom site for efficient and durable oxygen reduction catalysis, *J. Am. Chem. Soc.*, 2020, 141, 19800–19806.
- 24 X. Wang, X. Peng, W. Chen, Gu. Liu, A. Zheng, L. Zheng, J. Ni, C. Au and L. Jiang, The Insight into dynamic and steady-state active sites for nitrogen activation to ammonia by cobalt-based catalyst, *Nat. Commun.*, 2020, 11, 1–10.
- 25 H. Li, X. Li, J. Liang and Y. Chen, Hydrous RuO₂-decorated MXene coordinating with silver nanowire inks enabling fully printed micro-supercapacitors with extraordinary volumetric performance, Adv. Energy Mater., 2019, 9, 1–13.
- 26 P. Jiang, Y. Yang, R. Shi, G. Xia, J. Chen, J. Su and Q. Chen, Pt-like electrocatalytic behavior of Ru-MoO₂ nanocomposites for the hydrogen evolution reaction, *J. Mater. Chem. A*, 2017, 5, 5475–5485.
- 27 S. Musić, S. Popović, M. Maljković, K. Furić and A. Gajović, Formation of RuO₂ and Ru by thermal decomposition of ruthenium(III)-acetylacetonate, *J. Mater. Sci. Lett.*, 2002, 21, 1131–1134.
- 28 M. L. Green, M. E. Gross, L. E. Papa, K. J. Schnoes and D. Brasen, Chemical Vapor Deposition of Ruthenium and Ruthenium Dioxide Films, J. Electrochem. Soc., 1985, 132, 2677.
- 29 D. J. Martin, K. Qiu, S. A. Shevlin, A. D. Handoko, X. Chen, Z. Guo and J. Tang, Highly efficient photocatalytic H₂ evolution from water using visible light and structure-controlled graphitic carbon nitride, *Angew. Chem., Int. Ed.*, 2014, 53, 9240–9245.

- 30 Z. Ma, S. Zhao, X. Pei, X. Xiong and B. Hu, New insights into the support morphology-dependent ammonia synthesis activity of Ru/CeO₂ catalysts, *Catal. Sci. Technol.*, 2017, 7, 191–199.
- 31 B. Feng, C. Chen, H. Yang, X. Zhao, L. Hua, Y. Yu, T. Cao, Y. Shi and Z. Hou, Ionic liquid-promoted oxidant-free dehydrogenation of alcohols with water-soluble ruthenium nanoparticles in aqueous phase, *Adv. Synth. Catal.*, 2012, 354, 1559–1565.
- 32 D. J. Morgan, Resolving ruthenium: XPS studies of common ruthenium materials, *Surf. Interface Anal.*, 2015, 47, 1072–1079.
- 33 D. Briggs and G. Beamson, XPS studies of the oxygen 1s and 2s levels in a wide range of functional polymers, *Anal. Chem.*, 1993, **65**, 1517–1525.
- 34 A. Awati, H. Maimaiti, S. Wang and B. Xu, Photo-derived fixation of dinitrogen into ammonia at ambient condition with water on ruthenium/coal-based carbon nanosheets, *Sci. Total Environ.*, 2019, **695**, 133865.
- 35 Y. Liao, J. Lin, B. Cui, G. Xie and S. Hu, Well-dispersed ultrasmall ruthenium on TiO₂ (P25) for effective photocatalytic N₂ fixation in ambient condition, *J. Photochem. Photobiol.*, *A*, 2010, 387, 112100.
- 36 J. Ran, J. M. aroniec and S. Z. Qiao, Cocatalysts in semiconductor-based Photocatalytic CO₂ Reduction: achievements, challenges, and cpportunities, *Adv. Mater.*, 2018, 30, 1–31.
- 37 A. B. Jorge, D. J. Martin, M. T. S. Dhanoa, A. S. Rahman, N. Makwana, J. Tang, A. Sella, F. Corà, S. Firth, J. A. Darr and P. F. McMillan, H₂ and O₂ evolution from water half-splitting reactions by graphitic carbon nitride materials, *J. Phys. Chem. C*, 2013, 117, 7178–7185.
- 38 M. Kitano, Y. Inoue, Y. Yamazaki, F. Hayashi, S. Kanbara, S. Matsuishi, T. Yokoyama, S. Kim, M. Hara and H. Hosono, Ammonia synthesis using a stable electride as an electron donor and reversible hydrogen store, *Nat. Chem.*, 2012, 4, 934–940.